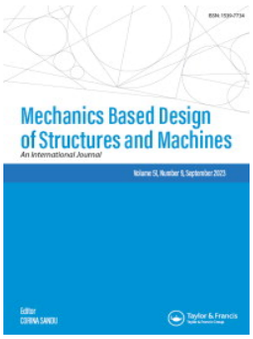

Taylor & Francis
Taylor & Francis Group

Mechanics Based Design of Structures and Machines
An International Journal

ISSN: (Print) (Online) Journal homepage: https://www.tandfonline.com/loi/lmbd20

Stress-Based topology optimization under the stress relaxation effect

Gil Ho Yoon, Meisam Takalloozadeh & Peyman Esmailpour

To cite this article: Gil Ho Yoon, Meisam Takalloozadeh & Peyman Esmailpour (2023) Stress-Based topology optimization under the stress relaxation effect, Mechanics Based Design of Structures and Machines, 51:9, 5141-5163, DOI: 10.1080/15397734.2021.1992776

To link to this article: https://doi.org/10.1080/15397734.2021.1992776

Published online: 25 Oct 2021.

MECHANICS BASED DESIGN OF STRUCTURES AND MACHINES
2023, VOL. 51, NO. 9, 5141–5163
https://doi.org/10.1080/15397734.2021.1992776

Taylor & Francis
Taylor & Francis Group

Stress-Based topology optimization under the stress relaxation effect

Gil Ho Yoon[a], Meisam Takalloozadeh[b,c], and Peyman Esmailpour[d]

[a]School of Mechanical Engineering, Hanyang University, Seoul, Republic of Korea; [b]Civil and Environmental Engineering Department, School of Engineering, Shiraz University, Shiraz, Iran; [c]School of Mechanical Engineering, Hanyang University, Seoul, Republic of Korea; [d]Civil and Environmental Engineering Department, School of Engineering, Shiraz University, Shiraz, Iran;

ABSTRACT

One of the effects of creep phenomena in structures is stress relaxation. Owing to this effect, the stiffness of each point is inversely related to the stress at that point, which causes a stress redistribution, a reduction of the maximum stress, and an increment in the displacement field. By contrast, for structural optimization, it is a practical and challenging problem to consider the maximum stress as a failure criterion or objective function. In the present study, the stress relaxation effect was investigated in stress-based topology optimization. The so-called solid isotropic material with penalization method and a nonlinear finite element analysis are utilized for this purpose. The maximum von Mises stress and the total volume of the structure are selected as the objective function and constraint, respectively. The main novelty of this research is to find the optimized topology with the least maximum stress by developing and implementing a time-dependent adjoint method for sensitivity analysis. Implementing the calculated sensitivity for stress-based problems in a gradient-based optimization method, such as the optimality criteria, is quite challenging, and some numerical instabilities in the optimization process are addressed. Several examples are solved with and without considering the stress relaxation effect. The results reveal that the influence of stress relaxation in the reduction of stress concentration makes the optimized layout more similar to the optimized layout obtained by minimizing the compliance for the linear structures.

ARTICLE HISTORY
Received 15 March 2021
Accepted 9 October 2021

KEYWORDS
Topology optimization; stress relaxation behavior; sensitivity analysis; stress constraint

1. Introduction

The real behaviors of various structures under different types of loading are almost nonlinear. However, they are mostly modeled with a linear relationship between stress and strain owing to their simplicity. In some cases, it is not possible to neglect the nonlinear behavior, which has a significant effect on the final result. Figure 1 presents the von Mises stress distribution in a sample 2D L-bracket structure with and without considering the nonlinear stress relaxation effect. As can be observed, owing to the stress relaxation, the maximum von Mises stress is reduced, and the stress field in the structure is redistributed. In this case, it is vital to consider the nonlinear effect. When the aim is to find the optimized layout using the maximum stress as a failure criterion or objective function, considering the aforementioned nonlinear behavior is more essential. This is the motivation for the present study.

Here, the nonlinearity is due to the nonlinear behavior of the material, which includes any inelastic behavior. Geometrical nonlinearity, which is a variation in the stiffness owing to large

CONTACT Meisam Takalloozadeh takalloozadeh@shirazu.ac.ir
Communicated by Makoto Ohsaki.

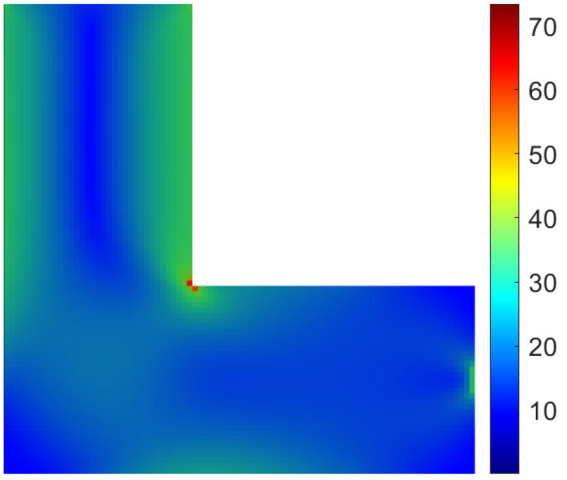

(a)

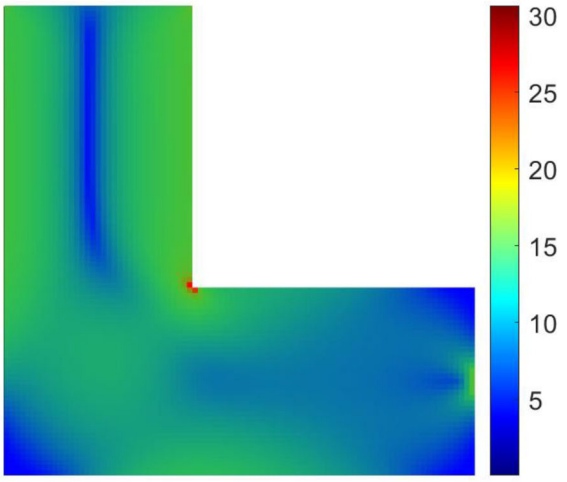

(b)

Figure 1. Von Mises stress field: (a) linear analysis and (b) nonlinear analysis under stress relaxation effect.

deformation, is another source of nonlinearity. Moreover, the nonlinearity can be due to the contact between different parts of the structures.

Creep, viscoelasticity, viscoplasticity, and fatigue are classified as rate-dependent material nonlinearities (Doghri 2013). This means that a nonlinear behavior is a function of the load history. By contrast, plasticity, nonlinear elasticity, and buckling are rate-independent nonlinear behaviors. In this study, the effect of stress relaxation owing to the presence of creep is investigated on the optimized layout of a structure. Stress relaxation is discussed in more detail in Section 2.1.

1.1. Stress-based topology optimization

Finding the best material distribution within the design domain is the aim of topology optimization. This field is expanding rapidly and has become the frontier of studies in structural

optimization. Furthermore, topology optimization is employed in various problems in physics and other engineering branches (Kook 2019). Since 1988 (Bendsoe and Kikuchi 1988), several methods have been applied different approaches in topology optimization (Eschenauer and Olhoff 2001, Maute and Sigmund 2013) the first of which is the homogenization method (Hassani and Hinton 1998b, Hassani and Hinton 1998a). This method was improved using one of the most popular approaches, solid isotropic material with penalization (SIMP) (Bendsøe 1989, Rozvany, Zhou, and Birker 1992) which uses the densities of the elements as design variables (Bendsoe and Sigmund 2013, Rozvany 2001). Level-set-based methods are another strategy in which the structural domain is defined by a level-set function (Allaire, Jouve, and Toader 2002, van Dijk et al. 2013).

The objective of most studies in structural topology optimization has been to find the optimized layout of a given volume fraction with the least compliance, which is called the compliance minimization problem. From an engineering perspective, stress plays an important role in the safety of structures. Therefore, stress-based topology optimization, in which the objective is to find the optimized layout of a given volume fraction with the least maximum stress, is more practical. However, solving these types of problems is difficult. In one of the earliest studies on this topic, Yang and Chen (Yang and Chen 1996) addressed two main problems. The first is a local quantity of stress that tends to have a large number of constraints. The P-norm method (Le et al. 2010) is an efficient and popular way to overcome this drawback and has been used in the present study. The second is instability owing to the high nonlinearity of stress with respect to the design variables. Another problem is in the SIMP method, which is called a singularity and has been discussed in numerous studies (Kirsch 1989, 1990, Cheng and Guo 1997, Guo, Cheng, and Yamazaki 2001, Bruggi 2008). A singularity is associated with zero-density elements that still have a strain leading to non-zero stress and occasionally significant when the level of stress should actually be zero (Holmberg, Torstenfelt, and Klarbring 2013). Gradient-based algorithms cannot find the global optimum for this non-convex problem. To remedy this situation, the stress constraints can be relaxed using several schemes such as ε-relaxation (Cheng and Guo 1997) or qp-relaxation (Bruggi 2008). Low-density elements cause an ill-conditioning of the stiffness matrixes, which may require more steps in the iterative solver and high computational costs (Wang, Sturler, and Paulino 2007).

Topology optimization considering stress constraints has also been employed in the level-set approach (Allaire and Jouve 2008, Amstutz and Novotny 2010) and has been utilized to find the optimized layout of a stress-based multi-material compliant mechanism problem (Chu, Gao, Xiao, Luo, and Li 2018). Because the stress constraint is applied only to the solid phase, there is no singularity problem in the level-set-based method. However, some other issues have been addressed (Guo et al. 2011, Suresh and Takalloozadeh 2013). For instance, the topological sensitivity typically flattens out far away from regions of high sensitivity that pose a numerical challenge during level-set extraction (Suresh and Takalloozadeh 2013). To have better control on the local stress, another research utilized an adaptive adjusting scheme of the stress penalty factor in the parametric level-set method and a new method is proposed based on stress penalty and adaptive volume constraint (Chu, Gao, Xiao, Luo, and Li 2018).

1.2. Nonlinearity in stress-based topology optimization

Topology optimization is being developed rapidly to evaluate the nonlinearity aspects of various problems. In structural topology optimization, most studies have focused on geometrical nonlinearity, particularly in mechanism problems, because the displacements are intrinsically large (Sigmund 1997, Kawamoto 2009). Stiffness maximization (compliance minimization) is the aim of most studies (Buhl, Pedersen, and Sigmund 2000). Earlier studies demonstrated that the optimized topology considering nonlinear effects can be significantly different from the topology for

minimal linear compliance (Swan and Kosaka 1997, Jung and Gea 2004). In addition to common difficulties in topology optimization for linear structures, several instabilities have been reported, mostly in a geometrical or nonlinear material analysis (Buhl, Pedersen, and Sigmund 2000, Lee and Park 2012). Moreover, in a sensitivity analysis for the SIMP method, Buhl et al. (Buhl, Pedersen, and Sigmund 2000) reported an indefinite or even negative definite tangent stiffness matrix in low-density elements owing to a large displacement. Several methods such as an equivalent static load, the removal of low-density elements, and a relaxation of the convergence criteria have been proposed to overcome these problems (Bruns and Tortorelli 2003, Buhl, Pedersen, and Sigmund 2000, Lee and Park 2012, Ahmad et al. 2017). Multi-scale topology optimization is another novel approach in nonlinear structural design (Nakshatrala, Tortorelli, and Nakshatrala 2013, Xia and Breitkopf 2014, Xia and Breitkopf 2016). Layering and islanding are other effects of void elements, and they were investigated by Luo et al. (Luo and Tong 2016). In a different approach, to remove spurious members in truss lattice topology optimization, a discrete filtering scheme was utilized (Zhang, Ramos, and Paulino 2017). Mesh distortion causes a divergence in the optimization process, which is an obstacle owing to the presence of low-density elements. The element connectivity parameterization (ECP) approach has proven to be efficient in overcoming this drawback (Yoon and Kim 2005, 2007).

Despite the aforementioned studies on compliance minimization, a few researchers have investigated nonlinearity in stress-based topology optimization. Here, the challenges of stress-based problems are added to the difficulties owing to nonlinearity. To achieve stress-based topology optimization for geometrically nonlinear structures using the ECP approach, the qp-relaxation method was developed (Moon and Yoon 2013). The ECP approach employs the link stiffness values for the connectivity among finite elements. Hence, it is powerful in solving topology optimization for geometrically nonlinear structures. Unified aggregation and relaxation methods were used to deal with stress constraints in the problem of a compliant mechanism (Capasso et al. 2020). Hyperelastic Neo-Hookean materials were adopted for nonlinear analysis. In another study, the stiffness of geometrically nonlinear structures was maximized, subject to the volume fraction and maximum von Mises stress constraints, by extending the bi-directional evolutionary structural optimization (Xu, Han, and Zhao 2020). This approach is based on adding and removing elements (discrete variables) and can effectively avoid the singularity problem in density-based methods. The filtering of topological variables has been used to stabilize the optimization process and highly nonlinear stress behaviors. Chi et al. incorporated material nonlinearity through tailored hyperelastic formulation, and topology optimization was conducted for the plane stress and plane strain conditions (Chi et al. 2019). Numerical examples have demonstrated the influence of various material behaviors. In addition to manufacturing uncertainty, geometric nonlinearity and stress constraints have been considered in compliant mechanism topology optimization (da Silva, Beck, and Sigmund 2020). To handle a large number of constraints, an augmented Lagrangian method is applied, and to overcome divergence issues owing to a large deformation in void regions, an energy interpolation scheme was employed.

Viscoelasticity as rate-dependent material nonlinearity has been studied sporadically, mostly as viscoelastic damping in topology optimization (Chen and Liu 2014). One of the common phenomena in rate-dependent material nonlinearity, particularly at high-temperature conditions, is creep. The theory of creep for different materials has been well developed (Betten 2008). However, there is a significant lack of studies when such effects as stress relaxation are considered in topology optimization. A linear viscoelastic model was utilized by James and Waisman (James and Waisman 2015) to obtain the optimized layout under viscoelastic creep deformation. The SIMP method and an adjoint method based on the Prony series function were used to define Young's modulus in a sensitivity analysis. A new approach for material nonlinearity based on the classical elastoplasticity model was utilized to avoid imposing a very large number of local stress constraints (Amir 2017). The author used the sensitivity analysis suggested by Michaleris

(Michaleris, Tortorelli, and Vidal 1994). The obtained layouts can sustain significantly higher loads than the layouts obtained from minimum compliance. In addition, creep is a complex function of stress, time, and temperature, and stress relaxation is one of the consequences of the dependency of stiffness on the stress owing to the creep phenomena. This effect was recently investigated in compliance minimization topology optimization (Takalloozadeh and Yoon 2019). The authors used the ECP approach and demonstrated the influence of stress relaxation on the optimized layouts.

In the present study, we investigate the effect of creep stress relaxation in a stress-constrained topology optimization problem. Alleviation of the maximum stress and an increase in the displacement field are calculated using a nonlinear finite element analysis, which is described in Section 2. In Section 3, the optimization formulation is given, and sensitivity analysis using a time-dependent adjoint method is derived. Section 4 deals with instabilities and solution methods. The results and discussion are presented in Section 5. Finally, some concluding remarks are given in Section 6.

2. Stress relaxation and nonlinear analysis

The theory of stress relaxation used in this study is presented in this section. The formulation is almost the same as the formulation which was provided in (Takalloozadeh and Yoon 2019). A nonlinear finite element analysis for considering the stress relaxation is then described.

2.1. Stress relaxation formulation

In general, the stress-strain relation owing to creep is time-dependent, and the strain is a function of stress, time, and temperature (Hetnarski, Reza Eslami, and Gladwell 2009). The behavior of the structures under creep can be split into three stages: primary (or transient), secondary, and tertiary. Most of the life of a structure is during the steady-state secondary stage, where the rate of strain ($\dot{\varepsilon}$) occurring as a result of creep can be expressed as a function of stress (σ):

$$\dot{\varepsilon}_{creep} = f(\sigma). \tag{1}$$

The above relation leads to an effect called stress relaxation, which has been investigated by many researchers. For metals and alloys, the rate of strain can be written as a power relation (Weertman 1955, Hetnarski, Reza Eslami, and Gladwell 2009):

$$\dot{\varepsilon}_{creep} = \alpha\sigma^{z}. \tag{2}$$

Here, parameters $.\alpha.$ and z are stress-independent material constant where the typical range for z in the annealed metals is between 1 and 7 (Tegart and Sherby 1958, Hetnarski, Reza Eslami, and Gladwell 2009). We used such a relationship in this study; however, other relations such as $\alpha\left(e^{\frac{\sigma}{\sigma_0}} - 1\right)$ and $\alpha(\sinh(\frac{\sigma}{\sigma_0}))^{z}$(Penny and Marriott 2012) can be used with no effect on the generality of the proposed optimization method. Here, σ_0 is a material constant independent of stress, but temperature-dependent. Based on a summation of the elastic and inelastic strains, the total strain at an arbitrary time ($t = t_f$) during the secondary stage of creep can be calculated as follows:

$$\varepsilon = \frac{\sigma}{E_0} + \alpha\sigma^{z}t_f = \sigma\left(\frac{1}{E_0} + \alpha\sigma^{z-1}t_f\right) \Rightarrow \frac{\sigma}{\varepsilon} = \frac{E_0}{1 + \alpha t_f E_0 \sigma^{z-1}} \Rightarrow E = \frac{E_0}{1 + \mu\sigma^{m}}. \tag{3}$$

Here, E_0 is the initial Young's modulus. For convenience in the calculations, $z - 1$ is replaced by m, and the coefficient of stress relaxation (α), E_0, and the desired time for the design (t_f) are combined in a constant parameter μ. Eq. (3) states that points with higher stress have a lower stiffness, which tends to redistribute the displacement and stress field. Although Eq. (3) is

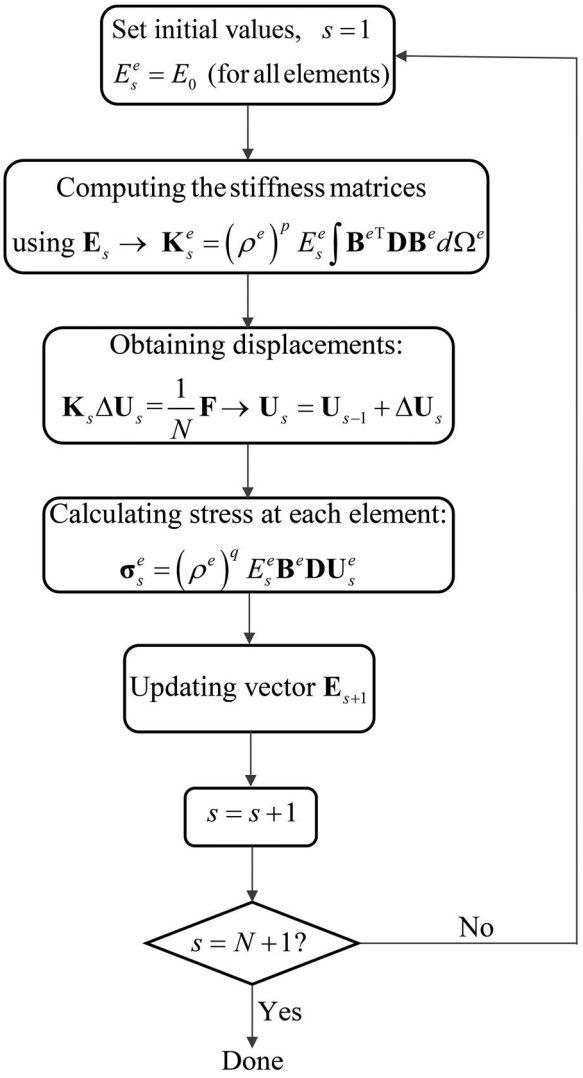

Figure 2. The schematic diagram for the nonlinear analysis algorithm.

obtained from the uniaxial test, it can be generalized for multi-axial stress states (Hayhurst 1972). The concept of the yield criterion, such as the von Mises criterion, can be used for the equivalent effects of multi-axial stress systems (Penny and Marriott 2012). It is worth mentioning that any relation between the stress and stiffness (not just the stress relaxation owing to creep) can be used instead of Eq. (3) with no effect on the generality of the rest of this study.

2.2. Nonlinear finite element implementation

Figure 2 presents a schematic diagram of the nonlinear finite element analysis to obtain the displacement ($\mathbf{U}$) and stress field. As shown, the applied force ($\mathbf{F}$) is gradually increased, and at each step, Young's modulus vector ($\mathbf{E}$) associated with the elements is updated using Eq. (3). The index s represents the number of steps in which displacement $\mathbf{U}_s$ is calculated, and the total number of steps is N. The stiffness matrix of each element ($\mathbf{K}_s^e$) while applying the SIMP method and considering the stress relaxation effect is obtained as follows:

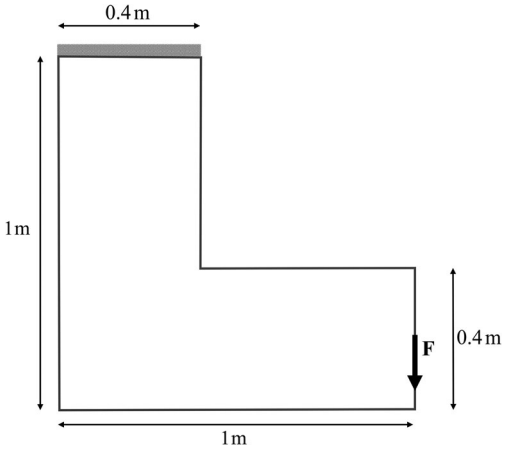

Figure 3. L-bracket problem.

$$\mathbf{K}_s^e = (\rho^e)^p E_s^e \int (\mathbf{B}^e)^{\mathrm{T}} \mathbf{D} \mathbf{B}^e d\Omega^e \,, E_s^e = \frac{E_0}{1 + \mu(\sigma_{s-1}^e)^m}. \tag{4}$$

Here, $\mathbf{D}$ is the material tensor, $\mathbf{B}$ represents the gradient matrix, and $.\rho^e.$ is the density of element number e, which is penalized by power p. For simplicity, in the rest of this paper, σ_s^e is used for the von Mises stress in the middle of the element e in step s. In 2D problems, the von Mises stress can be written in the form of the stress components (σ_{ij}):

$$\sigma^e = \sqrt{\sigma_{xx}^2 + \sigma_{yy}^2 - \sigma_{xx}\sigma_{yy} + 3\sigma_{xy}^2}. \tag{5}$$

Using the aforementioned algorithm, an L-bracket structure (Figure 3) under a unit concentrated load is analyzed. The initial Young's modulus $E_0 = 10^3\,\mathrm{N/m^2}$, and $\nu = 0.3$ is selected for the Poisson ratio, and the number of steps (N) in the nonlinear finite element is 10. Moreover, $\mu = 0.01$ and $m = 2$ are chosen to update Young's modulus. The von Mises stress distribution after the linear and nonlinear analyses is shown in Figure 1. Considering the stress relaxation effect, the maximum stress is reduced from $\sigma_{\max} = 73.37\,\mathrm{N/m^2}$ to $\sigma_{\max} = 30.63\,\mathrm{N/m^2}$, and regions with high stress are extended. Moreover, the displacement under the load point is increased from $u_{\max} = 0.1182\,\mathrm{m}$ to $u_{\max} = 0.1900\,\mathrm{m}$, which is an increment of more than 60%. Despite this increment in the displacement field, we still can use the assumption of small displacement to calculate the strain.

3. Problem definition and sensitivity analysis

The optimization problem in the present study can be mathematically formulated as follows:

$$\begin{aligned} &\text{Find } \boldsymbol{\rho} \\ &\text{Min}\left(\max \sigma_N^e\right) \\ &\text{Subject to :} \\ &|\Omega| = |\Omega|^* \\ &\mathbf{K}_s(\boldsymbol{\rho}, \mathbf{E}_s)\Delta\mathbf{U}_s = \Delta\mathbf{F}_s \; s = 1, 2, \ldots, N \end{aligned} \tag{6}$$

Here, Ω is a topology that must be computed within the design domain and $|\Omega|^*$ is the final volume fraction. In the following calculation, the subscripts denote the number of steps in the nonlinear finite element analysis, and the superscripts represent the number of elements.

3.1. Sensitivity analysis using the time-dependent adjoint method

To conduct a sensitivity analysis, the objective function, which is the maximum von Mises stress at the final step ($\max\sigma_N^e$), is added with the summation of the equilibrium equation at all steps multiplied by an arbitrary adjoint vector ($\boldsymbol{\lambda}_s$). Therefore, the objective function can be written as follows:

$$\psi = \max \sigma_N^e + \sum_{s=1}^{N} \boldsymbol{\lambda}_s^{\mathrm{T}} (\mathbf{K}_s \boldsymbol{\Delta}\mathbf{U}_s - \boldsymbol{\Delta}\mathbf{F}_s). \tag{7}$$

The P-norm function is used to make a differentiable function from the maximum von Mises stress (Le et al. 2010):

$$\psi = \left(\sum_{e=1}^{ne} \left(\sigma_N^e\right)^P \right)^{\frac{1}{P}} + \sum_{s=1}^{N} \boldsymbol{\lambda}_s^{\mathrm{T}} (\mathbf{K}_s \boldsymbol{\Delta}\mathbf{U}_s - \boldsymbol{\Delta}\mathbf{F}_s). \tag{8}$$

Here, ne is the total number of elements, and P in the P-norm relation should not be confused with power p in the SIMP method (Eq. (4)). Now, the sensitivity of the maximum von Mises stress with respect to the density of the j-th element (ρ^j) can be written as follows:

$$\frac{d\psi}{d\rho^j} = \left(\sum_e \left(\sigma_N^e\right)^P \right)^{\frac{1}{P}-1} \sum_e \left(\sigma_N^e\right)^{P-1} \frac{d\sigma_N^e}{d\rho^j} + \sum_s \boldsymbol{\lambda}_s^{\mathrm{T}} \left(\frac{d\mathbf{K}_s}{d\rho^j} \boldsymbol{\Delta}\mathbf{U}_s + \mathbf{K}_s \frac{d\boldsymbol{\Delta}\mathbf{U}_s}{d\rho^j} \right). \tag{9}$$

The first term in the above relation can be written in vector form, for which the following is more convenient:

$$\left(\sum_e \left(\sigma_N^e\right)^P \right)^{\frac{1}{P}-1} \sum_e \left(\sigma_N^e\right)^{P-1} \frac{d\sigma_N^e}{d\rho^j} = \mathbf{A} \left\{ \frac{d\sigma_N^1}{d\rho^j}, \ldots, \frac{d\sigma_N^e}{d\rho^j}, \ldots, \frac{d\sigma_N^{ne}}{d\rho^j} \right\}^{\mathrm{T}} = \mathbf{A} \frac{d\boldsymbol{\sigma}_N}{d\rho^j}. \tag{10}$$

where $\boldsymbol{\sigma}_N$ is a vector of size $ne \times 1$, representing von Mises values in the structural elements at step N, and vector $\mathbf{A}$ with the size of $1 \times ne$ is the following:

$$\mathbf{A} = \left(\sum_e \left(\sigma_N^e\right)^p \right)^{\frac{1}{p}-1} \left\{ \left(\sigma_N^1\right)^{p-1}, \ldots, \left(\sigma_N^e\right)^{p-1}, \ldots, \left(\sigma_N^{ne}\right)^{p-1} \right\}. \tag{11}$$

The von Mises stress at the step s in each element is obtained from the stress components ($\sigma_{xx,s}^e, \sigma_{yy,s}^e, \sigma_{xy,s}^e$) given in Eq. (5), and its differential can be expressed as follows:

$$\begin{aligned} d\sigma_s^e &= \frac{1}{2}\left(\sigma_s^e\right)^{-1} \begin{bmatrix} 2\left(\sigma_{xx,s}^e\right) d\sigma_{xx,s}^e + 2\left(\sigma_{yy,s}^e\right) d\sigma_{yy,s}^e \\ -d\left(\sigma_{xx,s}^e\right)\left(\sigma_{yy,s}^e\right) - \left(\sigma_{xx,s}^e\right) d\left(\sigma_{yy,s}^e\right) + 6\left(\sigma_{xy,s}^e\right) d\sigma_{xy,s}^e \end{bmatrix} \\ &= \frac{1}{2}\left(\sigma_s^e\right)^{-1} \left\{ 2\sigma_{xx,s}^e - \sigma_{yy,s}^e, 2\sigma_{yy,s}^e - \sigma_{xx,s}^e, 6\sigma_{xy,s}^e \right\} \begin{Bmatrix} d\sigma_{xx,s}^e \\ d\sigma_{yy,s}^e \\ d\sigma_{xy,s}^e \end{Bmatrix} = \mathbf{I}_s^e \begin{Bmatrix} d\sigma_{xx,s}^e \\ d\sigma_{yy,s}^e \\ d\sigma_{xy,s}^e \end{Bmatrix}. \end{aligned} \tag{12}$$

We introduced a new vector ($\mathbf{I}_s^e$) with a size of 1×3. The stress components are related to the nodal displacement ($\mathbf{U}_s^e$) as follows:

$$\begin{Bmatrix} \sigma_{xx,s}^e & \sigma_{yy,s}^e & \sigma_{xy,s}^e \end{Bmatrix}^{\mathrm{T}} = (\rho^e)^q E_s^e \mathbf{D}\mathbf{B}^e \mathbf{U}_s^e. \tag{13}$$

Here, we use different powers (q) for penalizing the density, which is proposed in the qp-relaxation method (Bruggi 2008). This issue is explained in more detail in Section 4. Hence, we obtain the following:

$$\begin{Bmatrix} d\sigma^e_{xx,s} \\ d\sigma^e_{yy,s} \\ d\sigma^e_{xy,s} \end{Bmatrix} = q(\rho^e)^{q-1}(d\rho^e)E^e_s\mathbf{DB}^e\mathbf{U}^e_s + (\rho^e)^q dE^e_s\mathbf{DB}^e\mathbf{U}^e_s + (\rho^e)^q E^e_s\mathbf{DB}^e d\mathbf{U}^e_s. \tag{14}$$

In summary,

$$\frac{d\sigma^e_N}{d\rho^j} = \frac{\partial\sigma^e_N}{\partial\rho^j} + \frac{\partial\sigma^e_N}{\partial E^e_N}\frac{dE^e_N}{d\rho^j} + \frac{\partial\sigma^e_N}{\partial\mathbf{U}^e_N}\frac{d\mathbf{U}^e_N}{d\rho^j} = b^e_N + g^e_N\frac{dE^e_N}{d\rho^j} + \mathbf{h}^e_N\frac{d\mathbf{U}^e_N}{d\rho^j} \tag{15}$$

In Eq. (15), some new parameters were used to simplify the rest of the calculations:

$$\begin{aligned} \frac{\partial\sigma^e_s}{\partial\rho^j} &= b^e_s = 0 \text{if} j \neq e \\ \frac{\partial\sigma^e_s}{\partial\rho^j} &= b^e_s = \mathbf{I}^e_s q(\rho^e)^{q-1}E^e_s\mathbf{DB}^e\mathbf{U}^e_s \text{if} j = e \end{aligned} \tag{16}$$

and

$$\frac{\partial\sigma^e_s}{\partial\mathbf{U}^e_s} = \mathbf{I}^e_s(\rho^e)^q E^e_s\mathbf{DB}^e = \mathbf{h}^e_s \tag{17}$$

$$\frac{\partial\sigma^e_s}{\partial E^e_s} = \mathbf{I}^e_s(\rho^e)^q\mathbf{DB}^e\mathbf{U}^e_s = \mathbf{h}^e_s\mathbf{U}^e_s = g^e_s. \tag{18}$$

Four-node quadrilateral elements were employed in this study; therefore, the number of degrees of freedom in each element is equal to eight, and the size of the vector $\mathbf{h}^e_s$ is 1×8. The Young's modulus in step s is the function of stress in the previous step, $s-1$; hence, the derivative of E^e_N in the second term in Eq. (15) is expressed as follows:

$$\frac{dE^e_N}{d\rho^j} = \frac{dE^e_N}{d\sigma^e_{N-1}}\frac{d\sigma^e_{N-1}}{d\rho^j} = \frac{dE^e_N}{d\sigma^e_{N-1}}\left(b^e_{N-1} + \mathbf{h}^e_{N-1}\frac{d\mathbf{U}^e_{N-1}}{d\rho^j} + g^e_{N-1}\frac{dE^e_{N-1}}{d\rho^j}\right). \tag{19}$$

Inserting Eq. (15) in Eq. (10) yields the following:

$$\mathbf{A}\frac{d\boldsymbol{\sigma}_N}{d\rho^j} = a_N + \mathbf{G}\frac{d\mathbf{E}_N}{d\rho^j} + \mathbf{H}\frac{d\mathbf{U}_N}{d\rho^j} = a_N + \mathbf{G}\frac{d\mathbf{E}_N}{d\rho^j} + \mathbf{H}\left(\sum_{r=1}^{N}\frac{d\boldsymbol{\Delta}\mathbf{U}_r}{d\rho^j}\right). \tag{20}$$

Here, the scalar a_N is a multiple of $\mathbf{A}$ in a vector, the elements of which are defined by b^e_N, the first term of Eq. (15), and $\mathbf{H} = \mathbf{A}\mathbf{h}_N$, where the elements of each vector in the matrix $\mathbf{h}_N$ are defined by Eq. (17). Finally, $\mathbf{G} = \mathbf{A} \odot \mathbf{g}_N$, where the e-th element of $\mathbf{g}_N$ is defined using Eq. (18) and $\odot$ indicates the Hadamard product. As described in Section 2, the displacement vector in step s is obtained by $\mathbf{U}_s = \sum_{r=1}^{s}\boldsymbol{\Delta}\mathbf{U}_r \Rightarrow \frac{d\mathbf{U}_s}{d\rho^j} = \sum_{r=1}^{s}\frac{d\boldsymbol{\Delta}\mathbf{U}_r}{d\rho^j}$. For the last step ($s = N$) and in vector and matrix forms, we obtain the following:

$$\frac{d\mathbf{E}_N}{d\rho^j} = \boldsymbol{\alpha}_N + \left[\boldsymbol{\beta}_N\frac{d\mathbf{U}_{N-1}}{d\rho^j}\right] + \boldsymbol{\gamma}_N \odot \frac{d\mathbf{E}_{N-1}}{d\rho^j} = \boldsymbol{\alpha}_N + \left[\boldsymbol{\beta}_N\left(\sum_{r=1}^{N-1}\frac{d\boldsymbol{\Delta}\mathbf{U}_r}{d\rho^j}\right)\right] + \boldsymbol{\gamma}_N \odot \frac{d\mathbf{E}_{N-1}}{d\rho^j}. \tag{21}$$

The e-th element of the newly defined vector, $\boldsymbol{\alpha}_N$, is $\frac{dE^e_N}{d\sigma^e_{N-1}} \times b^e_{N-1}$, and, therefore,

$$E^e_N = \frac{1}{1+\mu(\sigma^e_{N-1})^m} \Rightarrow \frac{dE^e_N}{d\sigma^e_{N-1}} = \frac{-m\mu(\sigma^e_{N-1})^{m-1}}{\left(1+\mu(\sigma^e_{N-1})^m\right)^2}. \tag{22}$$

In addition, $\boldsymbol{\beta}_N$ is a matrix where the elements of its column are defined as $\frac{dE^e_N}{d\sigma^e_{N-1}}\mathbf{h}^e_{N-1}$. Therefore, the number of rows is ne, and the number of columns is the number of degrees of

freedom. Moreover, $\boldsymbol{\gamma}_N$ is equal to $\boldsymbol{\beta}_N\left(\sum_{r=1}^{N-1}\frac{d\boldsymbol{\Delta}\mathbf{U}_r}{d\rho^j}\right)$. When the stress relaxation effect is used, the stiffness matrix is a function of both the densities of the elements and Young's modulus vector. Applying the chain rule, we obtain the following:

$$\mathbf{K}_s = \mathbf{K}_s\left(\rho^e, E_s^e\right) \Rightarrow \frac{d\mathbf{K}_s}{d\rho^j} = \frac{\partial \mathbf{K}_s}{\partial \rho^j} + \sum_{e=1}^{ne}\frac{\partial \mathbf{K}_s}{\partial E_s^e}\frac{dE_s^e}{d\rho^j} = \frac{\partial \mathbf{K}_s}{\partial \rho^j} + \sum_{e=1}^{ne}\frac{\partial \mathbf{K}_s}{\partial E_s^e}\frac{dE_s^e}{d\sigma_{s-1}^e}\frac{d\sigma_{s-1}^e}{d\rho^j}. \tag{23}$$

Inserting Eq. (19) into the above relation results in the following:

$$\frac{d\mathbf{K}_s}{d\rho^j} = \frac{\partial \mathbf{K}_s}{\partial \rho^j} + \sum_e \frac{\partial \mathbf{K}_s}{\partial E_s^e}\frac{dE_s^e}{d\sigma_{s-1}^e}\left(b_{s-1}^e + \mathbf{h}_{s-1}^e\frac{d\mathbf{U}_{s-1}^e}{d\rho^j} + g_{s-1}^e\frac{dE_{s-1}^e}{d\rho^j}\right), \tag{24}$$

Substituting Eq. (9) yields the following:

$$\begin{aligned}\frac{d\psi}{d\rho^j} = a_N + \mathbf{G}\left[\boldsymbol{\alpha}_N + \left[\boldsymbol{\beta}_N\left(\sum_{r=1}^{N-1}\frac{d\boldsymbol{\Delta}\mathbf{U}_r}{d\rho^j}\right)\right] + \boldsymbol{\gamma}_N \odot \frac{d\mathbf{E}_{N-1}}{d\rho^j}\right] + \mathbf{H}\left(\sum_{r=1}^{N}\frac{d\boldsymbol{\Delta}\mathbf{U}_r}{d\rho^j}\right)\\ + \sum_{s=1}^{N}\left(\boldsymbol{\lambda}_s^{\mathrm{T}}\frac{\partial \mathbf{K}_s}{\partial \rho^j}\boldsymbol{\Delta}\mathbf{U}_s + \boldsymbol{\lambda}_s^{\mathrm{T}}\sum_e\left(\frac{\partial \mathbf{K}_s}{\partial E_s^e}\frac{dE_s^e}{d\rho^j}\right)\boldsymbol{\Delta}\mathbf{U}_s + \boldsymbol{\lambda}_s^{\mathrm{T}}\mathbf{K}_s\frac{d\boldsymbol{\Delta}\mathbf{U}_s}{d\rho^j}\right).\end{aligned} \tag{25}$$

To avoid calculating $\frac{d\boldsymbol{\Delta}\mathbf{U}_N}{d\rho^j}$, the adjoint vector ($\boldsymbol{\lambda}_N$) should satisfy the following linear equation system:

$$\boldsymbol{\lambda}_N^{\mathrm{T}}\mathbf{K}_N + \mathbf{H} = \mathbf{0}. \tag{26}$$

According to the assembly equation, which yields a global stiffness matrix $\mathbf{K}_s$, we obtain $\frac{\partial \mathbf{K}_s}{\partial E_s^e} = \frac{\mathbf{k}_s^e}{E_s^e}$. Moreover, by defining $\boldsymbol{\eta}_s$ as $\sum_e\left(\boldsymbol{\lambda}_s^{\mathrm{T}}\frac{\partial \mathbf{K}_s}{\partial E_s^e}\boldsymbol{\Delta}\mathbf{U}_s\right)\frac{dE_s^e}{d\rho^j} = \boldsymbol{\eta}_s\frac{d\mathbf{E}_s}{d\rho^j}$, after calculating $\boldsymbol{\lambda}_N$, Eq. (25) can be written as follows:

$$\begin{aligned}\frac{d\psi}{d\rho^j} = a_N + \mathbf{G}\left[\boldsymbol{\alpha}_N + \left(\boldsymbol{\beta}_N\left(\sum_{r=1}^{N-1}\frac{d\boldsymbol{\Delta}\mathbf{U}_r}{d\rho^j}\right)\right) + \boldsymbol{\gamma}_N \odot \frac{d\mathbf{E}_{N-1}}{d\rho^j}\right] + \mathbf{H}\left(\sum_{r=1}^{N-1}\frac{d\boldsymbol{\Delta}\mathbf{U}_r}{d\rho^j}\right)\\ + \sum_{s=1}^{N}\left(\boldsymbol{\lambda}_s^{\mathrm{T}}\frac{\partial \mathbf{K}_s}{\partial \rho^j}\boldsymbol{\Delta}\mathbf{U}_s + \boldsymbol{\eta}_s\frac{d\mathbf{E}_s}{d\rho^j}\right) + \sum_{s=1}^{N-1}\boldsymbol{\lambda}_s^{\mathrm{T}}\mathbf{K}_s\frac{d\boldsymbol{\Delta}\mathbf{U}_s}{d\rho^j}.\end{aligned} \tag{27}$$

After simple calculations,

$$\begin{aligned}\frac{d\psi}{d\rho^j} = a_N + \mathbf{G}\boldsymbol{\alpha}_N + \sum_{s=1}^{N}\left(\boldsymbol{\lambda}_s^{\mathrm{T}}\frac{\partial \mathbf{K}_s}{\partial \rho^j}\boldsymbol{\Delta}\mathbf{U}_s\right) + \left(\mathbf{G}\boldsymbol{\beta}_N\left(\sum_{r=1}^{N-1}\frac{d\boldsymbol{\Delta}\mathbf{U}_r}{d\rho^j}\right)\right) + \mathbf{H}\left(\sum_{r=1}^{N-1}\frac{d\boldsymbol{\Delta}\mathbf{U}_r}{d\rho^j}\right)\\ + \mathbf{G}\boldsymbol{\gamma}_N \odot \frac{d\mathbf{E}_{N-1}}{d\rho^j} + \sum_{s=1}^{N}\left(\boldsymbol{\eta}_s\frac{d\mathbf{E}_s}{d\rho^j}\right) + \sum_{s=1}^{N-1}\boldsymbol{\lambda}_s^{\mathrm{T}}\mathbf{K}_s\frac{d\boldsymbol{\Delta}\mathbf{U}_s}{d\rho^j},\end{aligned} \tag{28}$$

where $\frac{d\mathbf{E}_s}{d\rho^j}$ can be calculated using Eq. (21) by replacing N with s, which is a recurrence relation, and, therefore,

$$\frac{d\psi}{d\rho^j} = a_N + \mathbf{G}\boldsymbol{\alpha}_N + \sum_{s=1}^{N}\left(\boldsymbol{\lambda}_s^{\mathrm{T}}\frac{\partial \mathbf{K}_s}{\partial \rho^j}\Delta\mathbf{U}_s\right) + \left(\mathbf{G}\boldsymbol{\beta}_N\left(\sum_{r=1}^{N-1}\frac{d\Delta\mathbf{U}_r}{d\rho^j}\right)\right) + \mathbf{H}\left(\sum_{r=1}^{N-1}\frac{d\Delta\mathbf{U}_r}{d\rho^j}\right) + \mathbf{G}\boldsymbol{\gamma}_N \odot \frac{d\mathbf{E}_{N-1}}{d\rho^j} + \boldsymbol{\eta}_N\left(\boldsymbol{\alpha}_N + \boldsymbol{\beta}_N\left(\sum_{r=1}^{N-1}\frac{d\Delta\mathbf{U}_r}{d\rho^j}\right) + \boldsymbol{\gamma}_N \odot \frac{d\mathbf{E}_{N-1}}{d\rho^j}\right) + \sum_{s=1}^{N-1}\left(\boldsymbol{\eta}_i\frac{d\mathbf{E}_i}{d\rho^j}\right) + \sum_{s=1}^{N-1}\boldsymbol{\lambda}_s^{\mathrm{T}}\mathbf{K}_s\frac{d\Delta\mathbf{U}_s}{d\rho^j} \tag{29}$$

Finally,

$$\frac{d\psi}{d\rho^j} = a_N + \mathbf{G}\boldsymbol{\alpha}_N + \sum_{s=1}^{N}\left(\boldsymbol{\lambda}_s^{\mathrm{T}}\frac{\partial \mathbf{K}_s}{\partial \rho^j}\Delta\mathbf{U}_s\right) + \left(\mathbf{G}\boldsymbol{\beta}_N\left(\sum_{r=1}^{N-1}\frac{d\Delta\mathbf{U}_r}{d\rho^j}\right)\right) + \mathbf{H}\left(\sum_{r=1}^{N-1}\frac{d\Delta\mathbf{U}_r}{d\rho^j}\right) + (\mathbf{G}+\boldsymbol{\eta}_N)\boldsymbol{\gamma}_N \odot \frac{d\mathbf{E}_{N-1}}{d\rho^j} + \boldsymbol{\eta}_N\left(\boldsymbol{\alpha}_N + \boldsymbol{\beta}_N\left(\sum_{r=1}^{N-1}\frac{d\Delta\mathbf{U}_r}{d\rho^j}\right)\right) + \sum_{s=1}^{N-1}\left(\boldsymbol{\eta}_s\frac{d\mathbf{E}_s}{d\rho^j}\right) + \sum_{s=1}^{N-1}\boldsymbol{\lambda}_s^{\mathrm{T}}\mathbf{K}_s\frac{d\Delta\mathbf{U}_s}{d\rho^j} \tag{30}$$

To eliminate the terms with coefficient $\frac{d\Delta\mathbf{U}_{N-1}}{d\rho^j}$, the following relation must be established:

$$\boldsymbol{\lambda}_{N-1}^{\mathrm{T}}\mathbf{K}_{N-1} + (\mathbf{G}+\boldsymbol{\eta}_N)\boldsymbol{\beta}_N + \mathbf{H} = \mathbf{0}. \tag{31}$$

Then, the rest of Eq. (30) will be as follows:

$$\frac{d\psi}{d\rho^j} = a_N + (\mathbf{G}+\boldsymbol{\eta}_N)\boldsymbol{\alpha}_N + \sum_{s=1}^{N}\left(\boldsymbol{\lambda}_s^{\mathrm{T}}\frac{\partial \mathbf{K}_s}{\partial \rho^j}\Delta\mathbf{U}_s\right) + ((\mathbf{G}+\boldsymbol{\eta}_N)\boldsymbol{\beta}_N + \mathbf{H})\left(\sum_{r=1}^{N-2}\frac{d\Delta\mathbf{U}_r}{d\rho^j}\right) + (\mathbf{G}+\boldsymbol{\eta}_N)\left(\boldsymbol{\gamma}_N \odot \frac{d\mathbf{E}_{N-1}}{d\rho^j}\right) + \boldsymbol{\eta}_{N-1}\frac{d\mathbf{E}_{N-1}}{d\rho^j} + \sum_{s=1}^{N-2}\left(\boldsymbol{\eta}_s\frac{d\mathbf{E}_s}{d\rho^j}\right) + \sum_{s=1}^{N-2}\boldsymbol{\lambda}_s^{\mathrm{T}}\mathbf{K}_s\frac{d\Delta\mathbf{U}_s}{d\rho^j} \tag{32}$$

One can continue these steps to calculate $\boldsymbol{\lambda}_{N-2}$ as follows:

$$\frac{d\psi}{d\rho^j} = a_N + (\mathbf{G}+\boldsymbol{\eta}_N)\boldsymbol{\alpha}_N + \sum_{s=1}^{N}\left(\boldsymbol{\lambda}_s^{\mathrm{T}}\frac{\partial \mathbf{K}_s}{\partial \rho^j}\Delta\mathbf{U}_s\right) + ((\mathbf{G}+\boldsymbol{\eta}_N)\boldsymbol{\beta}_N + \mathbf{H})\left(\sum_{r=1}^{N-2}\frac{d\Delta\mathbf{U}_r}{d\rho^j}\right) + (\mathbf{G}+\boldsymbol{\eta}_N)\left(\boldsymbol{\gamma}_N \odot \left(\boldsymbol{\alpha}_{N-1} + \boldsymbol{\beta}_{N-1}\left(\sum_{r=1}^{N-2}\frac{d\Delta\mathbf{U}_r}{d\rho^j}\right) + \boldsymbol{\gamma}_{N-1} \odot \frac{d\mathbf{E}_{N-2}}{d\rho^j}\right)\right) + \boldsymbol{\eta}_{N-1}\left(\boldsymbol{\alpha}_{N-1} + \boldsymbol{\beta}_{N-1}\left(\sum_{r=1}^{N-2}\frac{d\Delta\mathbf{U}_r}{d\rho^j}\right) + \boldsymbol{\gamma}_{N-1} \odot \frac{d\mathbf{E}_{N-2}}{d\rho^j}\right) + \sum_{s=1}^{N-2}\left(\boldsymbol{\eta}_s\frac{d\mathbf{E}_s}{d\rho^j}\right) + \sum_{s=1}^{N-2}\boldsymbol{\lambda}_s^{\mathrm{T}}\mathbf{K}_s\frac{d\Delta\mathbf{U}_s}{d\rho^j} \tag{33}$$

The summation of terms with $\frac{d\Delta\mathbf{U}_{N-2}}{d\rho^j}$ is set to zero, and thus,

$$\Rightarrow ((\mathbf{G}+\boldsymbol{\eta}_N)\boldsymbol{\beta}_N + \mathbf{H})\left(\frac{d\Delta\mathbf{U}_{N-2}}{d\rho^j}\right) + (\mathbf{G}+\boldsymbol{\eta}_N)\left(\boldsymbol{\gamma}_N \odot \left(\boldsymbol{\beta}_{N-1}\left(\frac{d\Delta\mathbf{U}_{N-2}}{d\rho^j}\right)\right)\right) + \boldsymbol{\eta}_{N-1}\left(\boldsymbol{\beta}_{N-1}\left(\frac{d\Delta\mathbf{U}_{N-2}}{d\rho^j}\right)\right) + \boldsymbol{\lambda}_{N-2}^{\mathrm{T}}\mathbf{K}_{N-2}\frac{d\Delta\mathbf{U}_{N-2}}{d\rho^j} = 0 \tag{34}$$

Therefore,

$$\Rightarrow \boldsymbol{\lambda}_{N-2}^{\mathrm{T}}\mathbf{K}_{N-2} + \left((\mathbf{G}+\boldsymbol{\eta}_N) \odot \boldsymbol{\gamma}_N^{\mathrm{T}} + \boldsymbol{\eta}_{N-1}\right)\boldsymbol{\beta}_{N-1} + (\mathbf{G}+\boldsymbol{\eta}_N)\boldsymbol{\beta}_N + \mathbf{H} = \mathbf{0}. \tag{35}$$

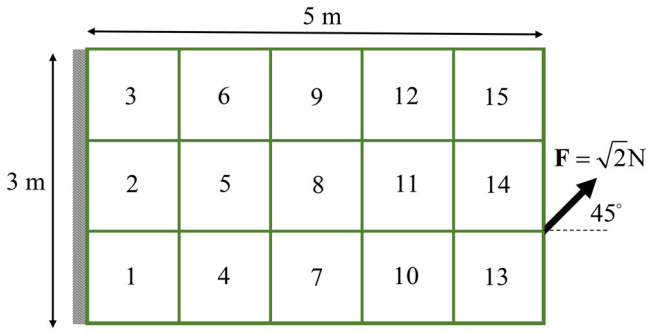

Figure 4. Cantilever beam with 15 elements.

The rest of the relation will be as follows:

$$\frac{d\psi}{d\rho^j} = a_N + (\mathbf{G}+\boldsymbol{\eta}_N)(\boldsymbol{\alpha}_N + \boldsymbol{\gamma}_N \odot \boldsymbol{\alpha}_{N-1}) + \boldsymbol{\eta}_{N-1}\boldsymbol{\alpha}_{N-1} + \sum_{s=1}^{N}\left(\boldsymbol{\lambda}_s^{\mathrm{T}}\frac{\partial \mathbf{K}_s}{\partial \rho^j}\boldsymbol{\Delta}\mathbf{U}_s\right)$$
$$+ \left((\mathbf{G}+\boldsymbol{\eta}_N)(\boldsymbol{\beta}_N + \boldsymbol{\gamma}_N \odot \boldsymbol{\beta}_{N-1}) + \boldsymbol{\eta}_{N-1}\boldsymbol{\beta}_{N-1} + \mathbf{H}\right)\left(\sum_{r=1}^{N-3}\frac{d\boldsymbol{\Delta}\mathbf{U}_r}{d\rho^j}\right)$$
$$+ (\mathbf{G}+\boldsymbol{\eta}_N)\left(\boldsymbol{\gamma}_N \cdot \boldsymbol{\gamma}_{N-1} \odot \frac{d\mathbf{E}_{N-2}}{d\rho^j}\right) + \boldsymbol{\eta}_{N-1}\left(\boldsymbol{\gamma}_{N-1} \odot \frac{d\mathbf{E}_{N-2}}{d\rho^j}\right) + \sum_{s=1}^{N-2}\left(\boldsymbol{\eta}_s\frac{d\mathbf{E}_s}{d\rho^j}\right) + \sum_{i=1}^{N-3}\boldsymbol{\lambda}_s^{\mathrm{T}}\mathbf{K}_s\frac{d\boldsymbol{\Delta}\mathbf{U}_s}{d\rho^j} \tag{36}$$

We can continue the calculation by computing $\boldsymbol{\lambda}_{N-3}$ into $\boldsymbol{\lambda}_1$, which is written as a loop in the programming code. After obtaining all adjoint vectors ($\boldsymbol{\lambda}_s$), one can calculate the desired derivative (Eq. (9)) by using the final relation that remains after the vanishing terms, including the derivative of the displacement ($\frac{d\boldsymbol{\Delta}\mathbf{U}_s}{d\rho^j}$). Moreover, the partial derivative of the global stiffness matrix can be easily obtained as follows:

$$\frac{\partial \mathbf{K}_s}{\partial \rho^j} = p\left(\rho^j\right)^{p-1}\mathbf{K}_s^j. \tag{37}$$

3.2. Verification using the finite difference method

Before utilizing the computed sensitivity in topology optimization, it is essential to verify it with the numerical results calculated using the finite difference method. The following central finite difference equation is used to compute the numerical derivative of the maximum von Mises stress ($\max\sigma_N^e$) with respect to the design variable ρ^j :

$$\frac{d}{d\rho^j}\max\sigma_N^e \approx \frac{\max\sigma_N^e\left(\rho^j + \Delta\rho^j\right) - \max\sigma_N^e\left(\rho^j - \Delta\rho^j\right)}{2\Delta\rho^j}. \tag{38}$$

The perturbation value of $\Delta\rho^j = 10^{-5}$ is used herein. A simple cantilever beam, shown in Figure 4 is discretized by 15 elements. The numbers of elements are given as well. The adopted material properties are $E = 10^3\ \mathrm{N/m^2}$, $\nu = 0.3$, $m = 2$, and $\mu = 0.01$.

Table 1 presents the results for the analytical and finite difference methods. A typical agreement of up to seven significant digits of precision is obtained, which proves the validity of the presented sensitivity analysis.

Table 1. Analytical sensitivity analysis and finite-difference results.

Element Number	Analytical	Finite difference
1	−4.735029714	−4.735029721
2	−0.687423538	−0.687423531
3	−0.911231758	−0.911231742
4	−0.82212429	−0.82212429
5	−0.095798682	−0.095798689
6	−0.305417047	−0.305417041
7	−0.062559274	−0.062559309
8	0.043764972	0.043764978
9	−0.028950754	−0.028950733
10	−0.018952006	−0.018951995
11	0.010596935	0.010596952
12	0.008785843	0.008785857
13	−0.005654223	−0.005654241
14	0.005924445	0.005924468
15	0.002581854	0.002581903

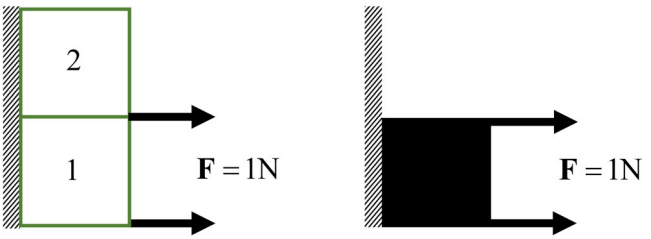

Figure 5. (a) Simple two element structure and (b) the expected optimum layout.

4. Convergence and stability of the optimization process

Assume a simple plate under tension, which is discretized into two elements (Figure 5-a). Under the given boundary conditions, the desired volume fraction equals 50% of the total volume, and the optimized layout for both linear and nonlinear structures is expected as shown in Figure 5-b. This means that two design variables should be obtained $\rho^1 = 1,\ \rho^2 = 0$. However, if we use the same penalization to compute the element stiffness matrix (Eq. (4)) and the stress in the elements (Eq. (13)), which means $q = p = 3,$ the 2D optimization space will be as shown in Figure 6-a. Here, $\mu = 0.01,$ and the Poisson ratio is zero. The vertical axis depicts the normalized maximum von Mises stress, and the horizontal axes are design variables. As can be observed, the gradient-based optimization methods do not converge to the desired optimum point. To overcome this difficulty, a different penalization can be used such that $q < p,$ which changes the optimization space, as displayed in Figure 6-b ($q = 2$) and Figure 6-c ($q = 0.5$). The greater slope obtained using $q = 0.5$ tends to achieve faster convergence during the optimization process. This technique which is called qp-relaxation was pointed in several studies for linear cases such as (Le et al. 2010). There is a similar problem for the nonlinear effects.

Another point that should be noted is the consideration of stress relaxation during the initial steps of the optimization process. With the SIMP method, the process initiates with a layout in which the densities are defined as follows: $\rho^e = |\Omega|^* \ e = 1, 2, \ldots, ne,$ and these values are raised to power $p,$ which makes them even smaller. This means that the stiffness of the elements is low during the initial steps. In addition, considering that the stress relaxation decreases the stiffness in most elements, during the initial steps, we might have instability in the nonlinear finite element analysis. Therefore, one can start with $\mu = 0$ and increase the parameter μ during the first steps of optimization to the determined value. Here, we use a linear increment.

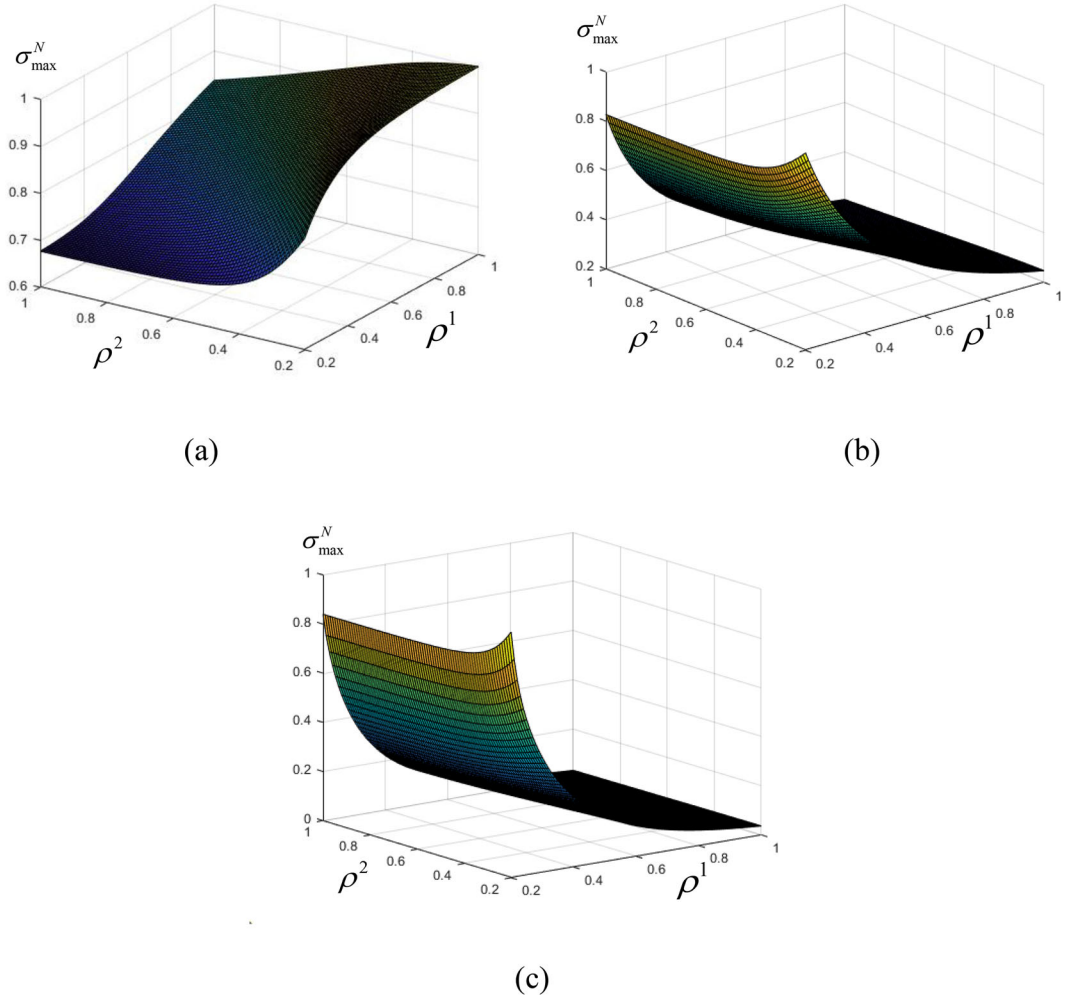

Figure 6. (a) Optimization space for $q = 3$, (b) $q = 2$, and (c) $q = 0.5$.

After calculating the required sensitivity, the direct Lagrange multiplier method (Kumar and Suresh 2021) is utilized to find the new design variables in the next step of the optimization process. This is faster than the bisection method with smoother convergence. The next technique that is used here is the selection of the movement parameter while applying the optimal criteria method, which should be smaller than the value that is usually used for linear problems. This is due to the greater complexity in the shape of the optimization space for nonlinear stress minimization problems.

To ensure the manufacturability and prevent numerical instabilities such as a checkerboard and mesh dependency, a modified filter with a Heaviside function is applied by modifying the densities of elements (Sigmund 2007):

$$\tilde{\rho}^e = e^{-\beta(1-\bar{\rho}^e)} - (1-\bar{\rho}^e)e^{-\beta}, \tag{39}$$

where $\bar{\rho}^e$ is the density filter introduced by Bourdin (Bourdin 2001) using elements in the neighborhood of element e (Ne):

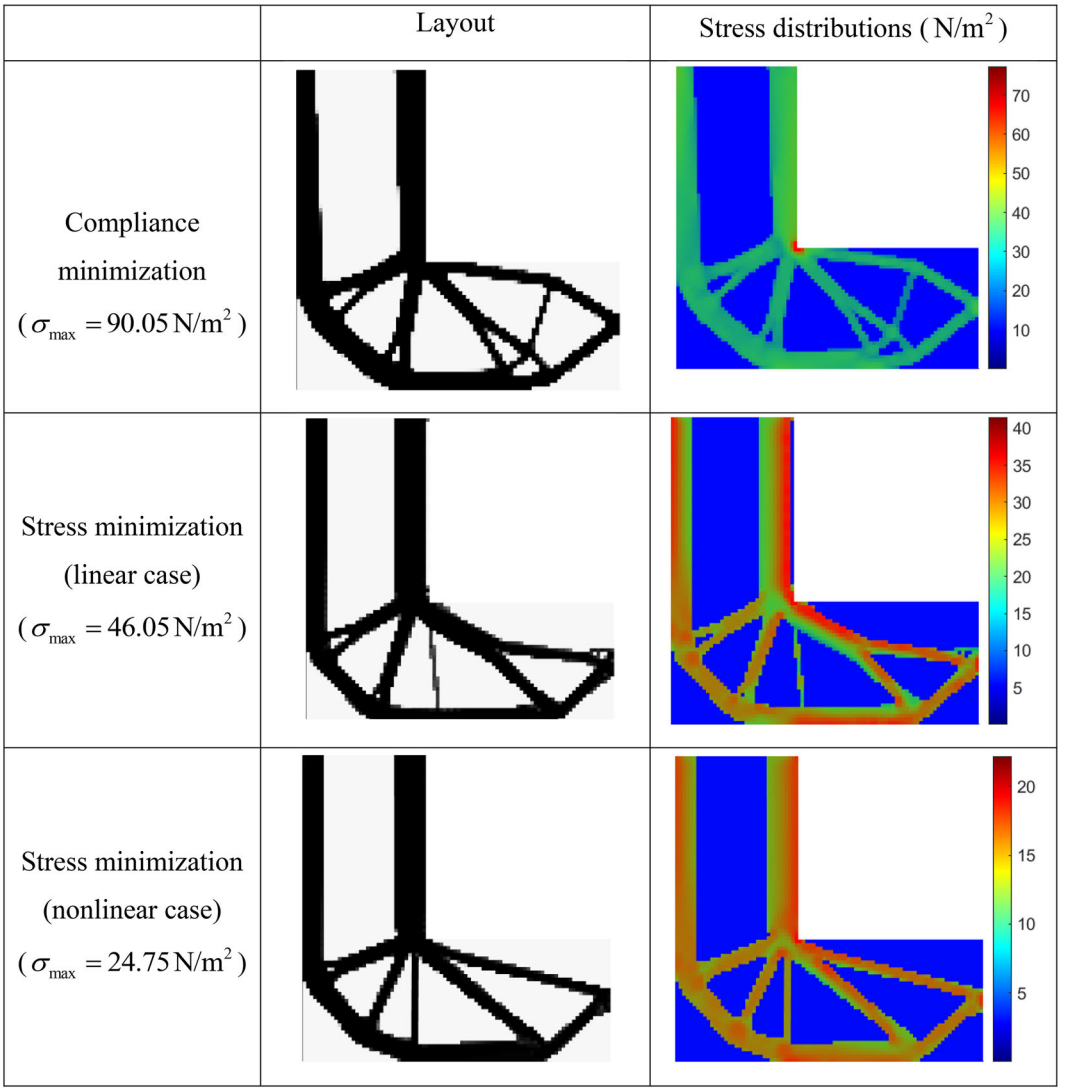

Figure 7. Optimized layouts and stress distribution in the optimum layouts for the L-bracket.

$$\bar{\rho}^e = \frac{\sum_{i \in Ne} w^i A^i \rho^i}{\sum_{i \in Ne} w^i A^i}. \tag{40}$$

Here, w^i is the weighting function that depends on the distance of elements i and e, and A^i is the volume of element i. The value of β is set to a small number and increases gradually during the optimization iteration. After using the filter for the element density, the element of the sensitivity vector should be modified as follows:

$$\frac{d\psi}{d\tilde{\rho}^e} = \frac{d\psi}{d\rho^e}\frac{d\rho^e}{d\tilde{\rho}^e}. \tag{41}$$

where $\frac{d\rho^e}{d\tilde{\rho}^e}$ is the inverse of the derivative of Eq. (40).

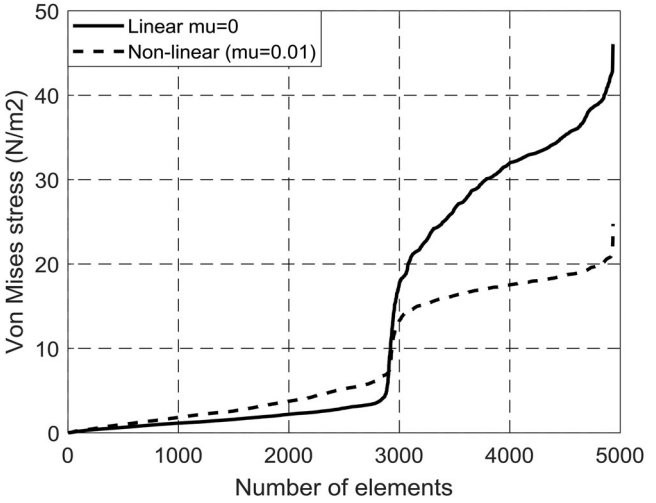

Figure 8. Von Mises stress in elements.

5. Results

Three examples have been considered to investigate the effect of stress relaxation on stress-based topology optimization. Without a loss of generality, Young's modulus and Poisson ratio were chosen to be $E = 10^3\ \mathrm{N/m^2}$ and $\nu = 0.3$, respectively. Moreover, the number of steps in the nonlinear FE analysis (N) is adopted as 10, and $m = 2$ in Eq. (3).

5.1. Example 1

The first example is the L-bracket structure illustrated in Figure 3 where the top of the structure is fixed, and a unit load is applied in the middle of the right side. This is one of the benchmark problems in stress-constrained topology optimization. Here, the design domain was discretized into 5000 elements, the mass limit was set to 40% of the total domain, and $P = 18$ in the P-norm relation (Eq. (8)). For linear structures and under compliance minimization, the optimized layout has a sharp corner with stress concentration, as shown in the first row of Figure 7 where the maximum von Mises stress is $\sigma_{\max} = 90.05\,\mathrm{N/m^2}$. An efficient stress minimization algorithm will lead to the optimized topology shown in the second row of Figure 7 which has the same volume and less maximum stress ($\sigma_{\max} = 46.05\,\mathrm{N/m^2}$) and lacks a sharp corner.

The optimized layout of the L-bracket problem considering a stress relaxation ($\mu = 0.01$) and using the proposed method is obtained and displayed in the third row of Figure 7. For comparison, the optimum design obtained for the linear case (Figure 7, second row) is reanalyzed under the stress relaxation effect ($\mu = 0.01$), and the objective function (Eq. (8)) is obtained, where $\psi = 29.73\,\mathrm{N/m^2}$, which is more than that in the optimized layout obtained by the proposed method ($\psi = 28.39\,\mathrm{N/m^2}$). This proves the efficiency of the algorithm to find the optimized layout considering the stress relaxation effect. It should be noted that the P-norm relation used in Eq. (8) is an approximation of the maximum stress. When stress values from which the maximum is calculated are more uniform, the P-norm value is less accurate and farther from the maximum value. Therefore, in the stress relaxation case, the difference between the objective function and the maximum von Mises stress is more than that in the linear case.

For the L-bracket structure, considering that stress relaxation reduces the stress concentration in the corner, the optimized layout (Figure 7, third row) is somewhat between the layout obtained during compliance minimization (Figure 7, first row) and stress minimization (Figure 7, second

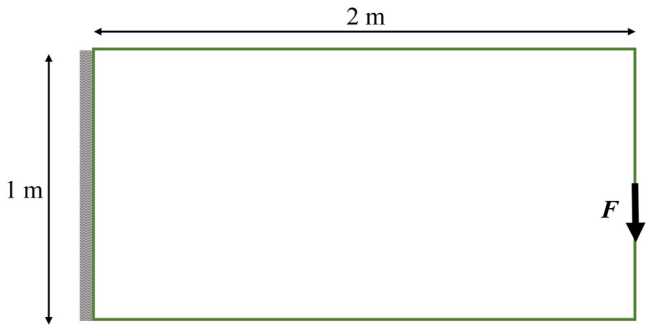

Figure 9. Cantilever beam problem.

	Layout	Stress distributions (N/m^2)
Compliance minimization $\sigma_{max} = 24.99\,N/m^2$		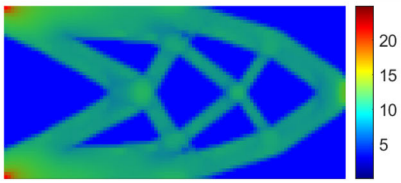
Stress minimization (linear case) $\sigma_{max} = 18.98\,N/m^2$	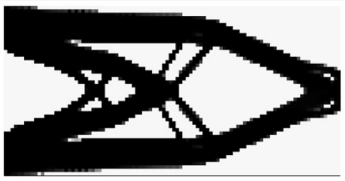	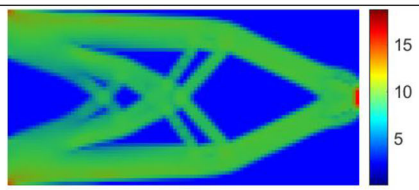
Stress minimization (nonlinear case) $\sigma_{max} = 10.43\,N/m^2$	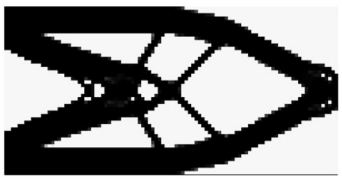	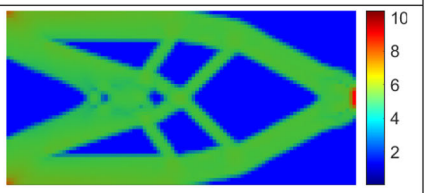

Figure 10. Optimized layouts and stress distribution in the optimum layouts for the cantilever beam.

row). The right vertical bar is completely located in the right part of the design domain (similar to Figure 7, first row), but there is no sharp corner (similar to Figure 7, second row). The difference between the linear and nonlinear cases is insignificant; nevertheless, the thickness and curvature of the bars are different.

The von Mises stress values in the elements are sorted and plotted for stress minimization layouts (Figure 7, second and third rows), as shown in Figure 8. In the nonlinear case, the stress values in the low-stress elements are more than those in the linear case and are less in high-stress elements, which makes the stress distribution more uniform in the optimized layout for the nonlinear case.

5.2. Example 2

In the second example, the optimized topology of a cantilever beam (Figure 9) is obtained. The beam is discretized into 100×50 elements, and a unit load is applied to the right side. Stress

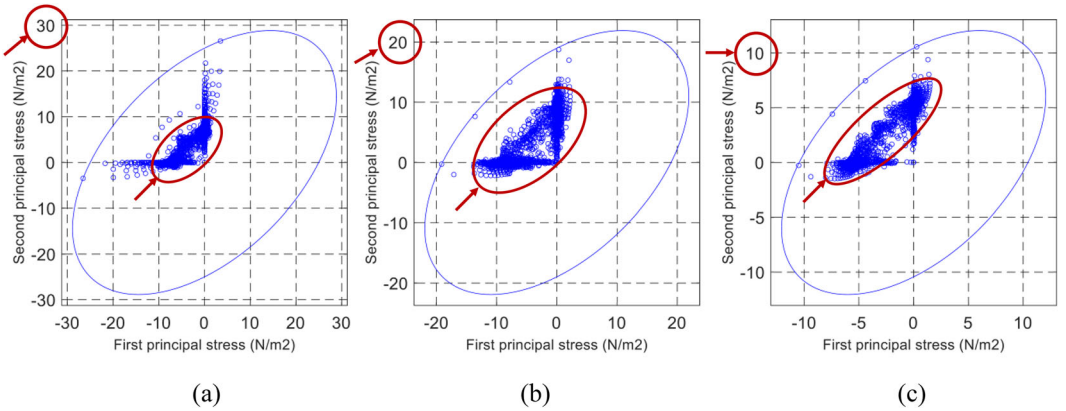

Figure 11. Principal stresses and 2D von Mises surface: (a) compliance minimization, linear case, (b) stress minimization, linear case, and (c) stress minimization, nonlinear case.

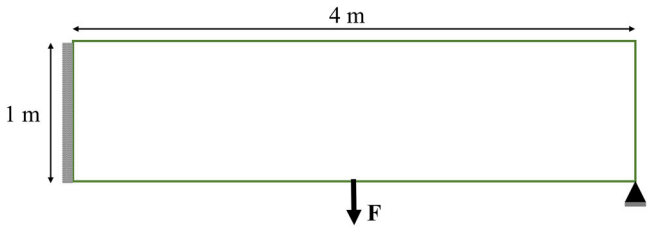

Figure 12. Cantilever beam with a support.

relaxation is considered using $\mu = 0.05$, where the volume fraction is 50%, and $P = 10$ for the P-norm relation. More values for P-norm mean more accuracy in calculating the maximum stress; however, it will lead to instability in the optimization process.

The optimized layouts for the different cases are shown in Figure 10. Similar to the last example, owing to the alleviation of stress under material nonlinearity behavior, the optimum layout for stress minimization (nonlinear case) is somewhat between compliance and stress minimization for the linear case. The stress field is more uniform, and the value of the maximum von Mises stress is less than the expected linear case. Considering a stress relaxation in compliance with the minimization for the cantilever problem led to an optimized layout with more structural bars than the optimized layout for the linear case (Takalloozadeh and Yoon 2019). However, this effect is not observed in the stress minimization design, and the number of structural elements is almost the same.

The principal stresses in the elements of optimized layouts are plotted on a 2D von Mises yield surface (Figure 11), where the yield surface in each graph is the maximum von Mises stress in the final layout. For the optimized layout in compliance minimization (Figure 11-a), the von Mises stresses in most elements are far from the maximum, which shows the stress concentration in a few elements. Utilizing the stress minimization algorithm for both linear and nonlinear cases gives layouts in which the stresses are distributed more uniformly and with fewer values for the maximum von Mises stress (Figure 11-b and c).

5.3. Example 3

The last example is another cantilever beam with extra pin support on the bottom-right side (Figure 12). A unit concentrated force is applied at the bottom middle of the beam, and the value for μ in the nonlinear case is selected as 0.01.

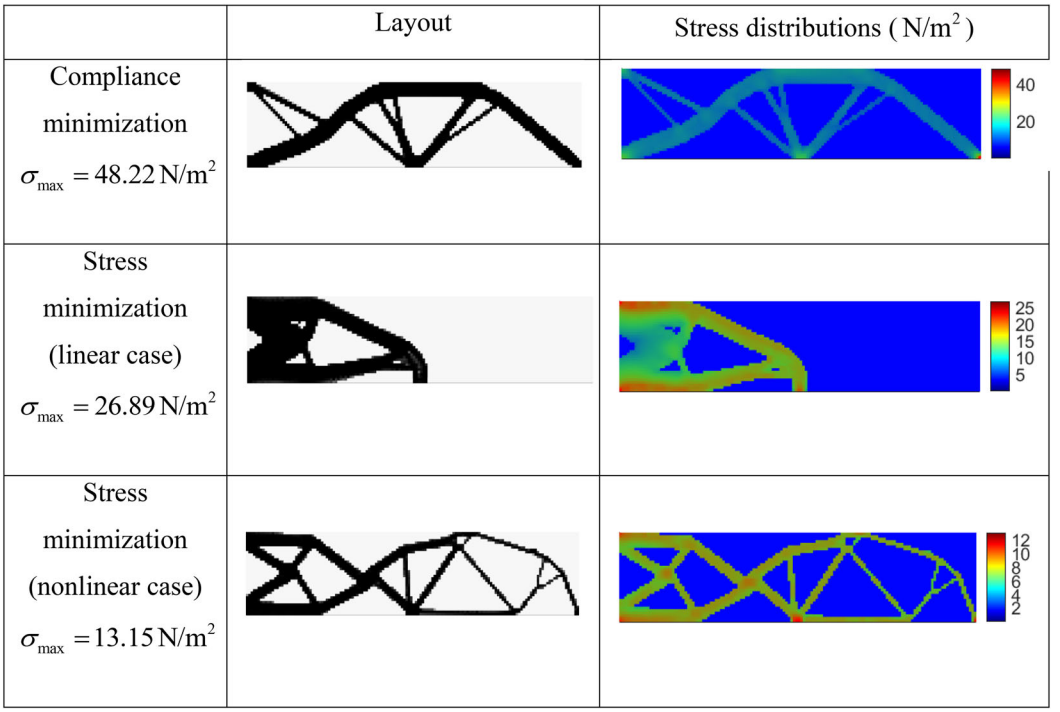

Figure 13. Optimized layouts and stress distribution in the optimum layouts for the cantilever beam with extra pin support.

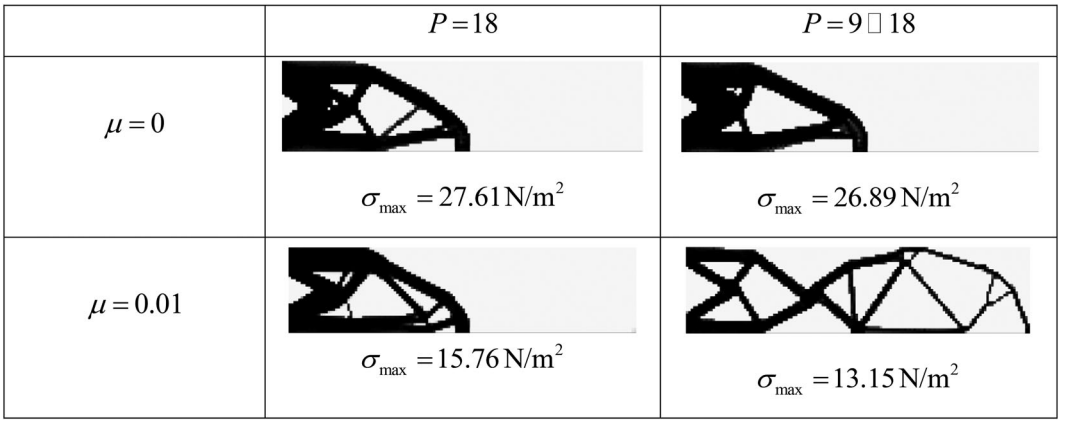

Figure 14. Optimized layouts using different techniques for the P-norm value.

The optimized layouts for compliance and stress minimization with and without considering the stress relaxation are shown in Figure 13. Here, the volume fraction is 30% of the design domain. In this example, the differences between linear and nonlinear optimized layouts are more significant. The optimized topology for the nonlinear case (Figure 13, last row) is more similar to a compliance minimization than a linear stress minimization.

Analyzing the optimized layout for the linear case (Figure 13, second row) under stress relaxation ($\mu = 0.01$) would give a maximum von Mises equal to $14.47\,N/m^2$. In comparison, the maximum von Mises stress for the layout obtained by the proposed method (Figure 13, third

row) is 13.15 N/m^2. Moreover, the value of the compliance for the optimum layout using compliance minimization is 14.0×10^{-3} J and for the stress minimization (linear case) is 35.4×10^{-3} J. This was expected since the objective function in the second problem is not compliance. For the stress minimization (nonlinear case), the compliance value is between two previous numbers and is equal to 21.0×10^{-3} J.

To obtain the optimized layout for stress minimization problems (Figure 13, second and third rows), the value of the P-norm is initially set to 9 and increases gradually to 18 during the first optimization steps (e.g., 100 steps). This technique led to better results. The comparison between optimized layouts using constant and dynamic P-norm values is given in the second column in Figure 14 and the third column in Figure 14, respectively. For both cases, using the dynamic technique in increasing P-norm gives layouts with less maximum von Mises stress. However, the effectiveness of the technique and choosing the appropriate range for the P-norm in the other problems for linear and nonlinear cases should be further investigated.

6. Conclusion

In this study, the effects of stress relaxation on the optimized topology of the structures were investigated. The optimized layouts were obtained by minimizing the maximum von Mises stress, whereas a nonlinear analysis considering the stress relaxation was conducted. The time-dependent adjoint method was used to calculate the sensitivity of the maximum von Mises stress with respect to the element density.

In comparison to the effect of stress relaxation in compliance minimization problems, the results show that the influence of stress relaxation on the optimized layout in stress minimization problems was less. This could be due to the stress alleviation in the structures. Stress relaxation decreases the stress concentration and the maximum von Mises stress. Therefore, the optimized layout for the stress minimization problem under the nonlinear stress relaxation effect is almost a layout between the optimized layout obtained in linear stress minimization and the optimized layout obtained in linear compliance minimization. However, there are differences in the thickness and curvature of the layouts. One of the common layouts in optimized topologies considering material nonlinearity is the existence of more structural bars in comparison with linear structures. This is not observed in the stress-based design under the stress relaxation effect, and the number of structural elements is almost the same.

To obtain the optimized layout and avoid several instabilities and non-optimal layouts, several methods were employed. In addition to common methods such as qp-relaxation and a density filter, in particular, the effect of nonlinearity is increased gradually in the first steps of the optimization process. Moreover, we found that the same technique for increasing the P-norm value will lead to better results in most stress-based problems.

Replication of results

For the replication of the results, details have been provided in Sections 2, 3, and 4, including sensitivity analysis and numerical techniques to overcome instabilities. Besides, the boundary conditions and the number of elements for the examples are provided in Section 5.

Moreover, the authors have provided the codes for the sensitivity analysis (in content-obscured, executable files) so that the readership can replicate the result in Table 1 and also use them to solve different problems with different geometry, boundary conditions, and material properties. However, if the provided information is not enough, we sincerely welcome you to contact us for further explanation.

Funding

This work was supported by the Korea Institute of Energy Technology Evaluation and Planning (KETEP) grant funded by the Korean government (MOTIE). (2021202080026D, Development of platform technology and operation management system for design and operating condition diagnosis of fluid machinery with variable devices based on AI/ICT).

ORCID

Meisam Takalloozadeh http://orcid.org/0000-0003-1193-600X

References

Ahmad, Z., T. Sultan, M. Zoppi, M. Abid, and G. J. Park. 2017. Nonlinear response topology optimization using equivalent static loads-case studies. *Engineering Optimization* 49 (2):252–68. doi:10.1080/0305215X.2016.1187728.

Allaire, G., and F. Jouve. 2008. Minimum stress optimal design with the level set method. *Engineering Analysis with Boundary Elements* 32 (11):909–18. doi:10.1016/j.enganabound.2007.05.007.

Allaire, G., F. Jouve, and A.-M. Toader. 2002. A level-set method for shape optimization. *Comptes Rendus Mathematique* 334 (12):1125–30. doi:10.1016/S1631-073X(02)02412-3.

Amir, O. 2017. Stress-constrained continuum topology optimization: a new approach based on elasto-plasticity. *Structural and Multidisciplinary Optimization* 55 (5):1797–818. doi:10.1007/s00158-016-1618-8.

Amstutz, S., and A. A. Novotny. 2010. Topological optimization of structures subject to von Mises stress constraints. *Structural and Multidisciplinary Optimization* 41 (3):407–20. doi:10.1007/s00158-009-0425-x.

Bendsøe, M. P. 1989. Optimal shape design as a material distribution problem. *Structural Optimization* 1 (4): 193–202. doi:10.1007/BF01650949.

Bendsoe, M. P., and N. Kikuchi. 1988. Generating optimal topologies in structural design using a homogenization method. *Computer Methods in Applied Mechanics and Engineering* 71 (2):197–224.

Bendsoe, M. P., and O. Sigmund. 2013. *Topology optimization: Theory, methods, and applications*. Berlin; Heidelberg: Springer Science & Business Media.

Betten, J. 2008. *Creep mechanics*. Berlin; Heidelberg: Springer Science & Business Media.

Bourdin, B. 2001. Filters in topology optimization. *International Journal for Numerical Methods in Engineering* 50 (9):2143–58. doi:10.1002/nme.116.

Bruggi, M. 2008. On an alternative approach to stress constraints relaxation in topology optimization. *Structural and Multidisciplinary Optimization* 36 (2):125–41. doi:10.1007/s00158-007-0203-6.

Bruns, T. E., and D. A. Tortorelli. 2003. An element removal and reintroduction strategy for the topology optimization of structures and compliant mechanisms. *International Journal for Numerical Methods in Engineering* 57 (10):1413–30. doi:10.1002/nme.783.

Buhl, T., C. B. Pedersen, and O. Sigmund. 2000. Stiffness design of geometrically nonlinear structures using topology optimization. *Structural and Multidisciplinary Optimization* 19 (2):93–104. doi:10.1007/s001580050089.

Capasso, G., J. Morlier, M. Charlotte, and S. Coniglio. 2020. Stress-based topology optimization of compliant mechanisms using nonlinear mechanics. *Mechanics & Industry* 21 (3):304– 17. doi:10.1051/meca/2020011.

Chen, W. J., and S. T. Liu. 2014. Topology optimization of microstructures of viscoelastic damping materials for a prescribed shear modulus. *Structural and Multidisciplinary Optimization* 50 (2):287–96. doi:10.1007/s00158-014-1049-3.

Cheng, 22 G., and X. Guo. 1997. ε-relaxed approach in structural topology optimization. *Structural Optimization* 13 (4):258–66. doi:10.1007/BF01197454.

Chi, H., D. L. Ramos, A. S. Ramos, Jr, and G. H. Paulino. 2019. On structural topology optimization considering material nonlinearity: Plane strain versus plane stress solutions. *Advances in Engineering Software* 131:217–31. doi:10.1016/j.advengsoft.2018.08.017.

Chu, S., L. Gao, M. Xiao, Z. Luo, and H. Li. 2018. Stress-based multi-material topology optimization of compliant mechanisms. *International Journal for Numerical Methods in Engineering* 113 (7):1021–44. doi:10.1002/nme.5697.

Chu, S., L. Gao, M. Xiao, Z. Luo, H. Li, and X. Gui. 2018. A new method based on adaptive volume constraint and stress penalty for stress-constrained topology optimization. *Structural and Multidisciplinary Optimization* 57 (3):1163–85. doi:10.1007/s00158-017-1803-4.

da Silva, G. A., A. T. Beck, and O. Sigmund. 2020. Topology optimization of compliant mechanisms considering stress constraints, manufacturing uncertainty and geometric nonlinearity. *Computer Methods in Applied Mechanics and Engineering* 365:112972. doi:10.1016/j.cma.2020.112972.

Doghri, I. 2013. *Mechanics of deformable solids: Linear, nonlinear, analytical and computational aspects*. Berlin; Heidelberg: Springer Science & Business Media.

Eschenauer, H. A., and N. Olhoff. 2001. Topology optimization of continuum structures: A review. *Applied Mechanics Reviews* 54 (4):331–90. doi:10.1115/1.1388075.

Guo, X., G. Cheng, and K. Yamazaki. 2001. A new approach for the solution of singular optima in truss topology optimization with stress and local buckling constraints. *Structural and Multidisciplinary Optimization* 22 (5): 364–73. doi:10.1007/s00158-001-0156-0.

Guo, X., W. S. Zhang, M. Y. Wang, and P. Wei. 2011. Stress-related topology optimization via level set approach. *Computer Methods in Applied Mechanics and Engineering* 200 (47-48):3439–52. doi:10.1016/j.cma.2011.08.016.

Hassani, B., and E. Hinton. 1998a. A review of homogenization and topology optimization II - analytical and numerical solution of homogenization equations. *Computers & Structures* 69 (6):719–38. doi:10.1016/S0045-7949(98)00132-1.

Hassani, B., and E. Hinton. 1998b. A review of homogenization and topology optimization I—homogenization theory for media with periodic structure. *Computers & Structures* 69 (6):707–17. doi:10.1016/S0045-7949(98)00131-X.

Hayhurst, D. R. 1972. Creep rupture under multi-axial states of stress. *Journal of the Mechanics and Physics of Solids* 20 (6):381–2. doi:10.1016/0022-5096(72)90015-4.

Hetnarski, R. B., M. Reza Eslami, and G. M. L. Gladwell. 2009. *Thermal Stresses: advanced Theory and Applications*. Vol. 41. Netherlands: Springer.

Holmberg, E., B. Torstenfelt, and A. Klarbring. 2013. Stress constrained topology optimization. *Structural and Multidisciplinary Optimization* 48 (1):33–47. doi:10.1007/s00158-012-0880-7.

James, K. A., and H. Waisman. 2015. Topology optimization of viscoelastic structures using a time-dependent adjoint method. *Computer Methods in Applied Mechanics and Engineering* 285:166–87. doi:10.1016/j.cma.2014.11.012.

Jung, D., and H. C. Gea. 2004. Topology optimization of nonlinear structures. *Finite Elements in Analysis and Design* 40 (11):1417–27. doi:10.1016/j.finel.2003.08.011.

Kawamoto, A. 2009. Stabilization of geometrically nonlinear topology optimization by the Levenberg-Marquardt method. *Structural and Multidisciplinary Optimization* 37 (4):429–33. doi:10.1007/s00158-008-0236-5.

Kirsch, U. 1989. Optimal topologies of truss structures. *Computer Methods in Applied Mechanics and Engineering* 72 (1):15–28. doi:10.1016/0045-7825(89)90119-9.

Kirsch, U. 1990. On singular topologies in optimum structural design. *Structural Optimization* 2 (3):133–42. doi:10.1007/BF01836562.

Kook, J. 2019. Evolutionary topology optimization for acoustic-structure interaction problems using a mixed u/p formulation. *Mechanics Based Design of Structures and Machines* 47 (3):356–74. doi:10.1080/15397734.2018.1557527.

Kumar, T., and K. Suresh. 2021. Direct Lagrange multiplier updates in topology optimization revisited. *Structural and Multidisciplinary Optimization* 63 (3):1563–16. doi:10.1007/s00158-020-02740-y.

Le, C., J. Norato, T. Bruns, C. Ha, and D. Tortorelli. 2010. Stress-based topology optimization for continua. *Structural and Multidisciplinary Optimization* 41 (4):605–20. doi:10.1007/s00158-009-0440-y.

Lee, H.-A., and G.-J. Park. 2012. Topology optimization for structures with nonlinear behavior using the equivalent static loads method. *Journal of Mechanical Design* 134 (3):031004. doi:10.1115/1.4005600.

Luo, Q. T., and L. Y. Tong. 2016. An algorithm for eradicating the effects of void elements on structural topology optimization for nonlinear compliance. *Structural and Multidisciplinary Optimization* 53 (4):695–714. doi:10.1007/s00158-015-1325-x.

Maute, K., O. Sigmund. 2013. Topology optimization approaches: a comparative review. *Structural, and Multidisciplinary Optimization* 6: 1031–55.

Michaleris, P., D. A. Tortorelli, and C. A. Vidal. 1994. Tangent operators and design sensitivity formulations for transient non-linear coupled problems with applications to elastoplasticity. *International Journal for Numerical Methods in Engineering* 37 (14):2471–99. doi:10.1002/nme.1620371408.

Moon, S. J., and G. H. Yoon. 2013. A newly developed qp-relaxation method for element connectivity parameterization to achieve stress-based topology optimization for geometrically nonlinear structures. *Computer Methods in Applied Mechanics and Engineering* 265:226–41. doi:10.1016/j.cma.2013.07.001.

Nakshatrala, P. B., D. A. Tortorelli, and K. B. Nakshatrala. 2013. Nonlinear structural design using multiscale topology optimization. Part I: Static formulation. *Computer Methods in Applied Mechanics and Engineering* 261-262:167–76. doi:10.1016/j.cma.2012.12.018.

Penny, R. K., and D. L. Marriott. 2012. *Design for creep*. Netherlands: Springer Science & Business Media.

Rozvany, G. I. N. 2001. Aims, scope, methods, history and unified terminology of computer-aided topology optimization in structural mechanics. *Structural and Multidisciplinary Optimization* 21 (2):90–108. doi:10.1007/s001580050174.

Rozvany, G. I., M. Zhou, and T. Birker. 1992. Generalized shape optimization without homogenization. *Structural Optimization* 4 (3-4):250–2. doi:10.1007/BF01742754.

Sigmund, O. 1997. On the design of compliant mechanisms using topology optimization. *Mechanics of Structures and Machines* 25 (4):493–524. doi:10.1080/08905459708945415.

Sigmund, O. 2007. Morphology-based black and white filters for topology optimization. *Structural and Multidisciplinary Optimization* 33 (4-5):401–24. doi:10.1007/s00158-006-0087-x.

Suresh, K., and M. Takalloozadeh. 2013. Stress-constrained topology optimization: A topological level-set approach. *Structural and Multidisciplinary Optimization* 48 (2):295–309. doi:10.1007/s00158-013-0899-4.

Swan, C. C., and I. Kosaka. 1997. Voigt-Reuss topology optimization for structures with linear elastic material behaviours. *International Journal for Numerical Methods in Engineering* 40 (16):3033–57. doi:10.1002/(SICI)1097-0207(19970830)40:16<3033::AID-NME196>3.0.CO;2-Z.

Takalloozadeh, M., and G. H. Yoon. 2019. Topology Optimization Under Stress Relaxation Effect Using Internal Element Connectivity Parameterization. *Journal of Computational and Nonlinear Dynamics* 14 (2):021006. doi:10.1115/1.4041578.

Tegart, W. M., and O. D. Sherby. 1958. Activation energies for high temperature creep of polycrstalline zinc. *Philosophical Magazine* 3 (35):1287–96. doi:10.1080/14786435808233311.

van Dijk, N. P., K. Maute, M. Langelaar, and F. van Keulen. 2013. Level-set methods for structural topology optimization: A review. *Structural and Multidisciplinary Optimization* 48 (3):437–72. doi:10.1007/s00158-013-0912-y.

Wang, S., E. d Sturler, and G. H. Paulino. 2007. Large-scale topology optimization using preconditioned Krylov subspace methods with recycling. *International Journal for Numerical Methods in Engineering* 69 (12):2441–68. doi:10.1002/nme.1798.

Weertman, J. 1955. Theory of steady-state creep based on dislocation climb. *Journal of Applied Physics* 26 (10):1213–7. doi:10.1063/1.1721875.

Xia, L., and P. Breitkopf. 2014. A reduced multiscale model for nonlinear structural topology optimization. *Computer Methods in Applied Mechanics and Engineering* 280:117–34. doi:10.1016/j.cma.2014.07.024.

Xia, L., and P. Breitkopf. 2016. Recent advances on topology optimization of multiscale nonlinear structures. *Archives of Computational Methods in Engineering* 2 (24):227–49.

Xu, B., Y. Han, and L. Zhao. 2020. Bi-directional evolutionary topology optimization of geometrically nonlinear continuum structures with stress constraints. *Applied Mathematical Modelling* 80:771–91. doi:10.1016/j.apm.2019.12.009.

Yang, R. J., and C. J. Chen. 1996. Stress-based topology optimization. *Structural Optimization* 12 (2-3):98–105. doi:10.1007/BF01196941.

Yoon, G. H., and Y. Y. Kim. 2005. Element connectivity parameterization for topology optimization of geometrically nonlinear structures. *International Journal of Solids and Structures* 42 (7):1983–2009. doi:10.1016/j.ijsolstr.2004.09.005.

Yoon, G. H., and Y. Y. Kim. 2007. Topology optimization of material-nonlinear continuum structures by the element connectivity parameterization. *International Journal for Numerical Methods in Engineering* 69 (10):2196–218. doi:10.1002/nme.1843.

Zhang, X., A. S. Ramos, and G. H. Paulino. 2017. Material nonlinear topology optimization using the ground structure method with a discrete filtering scheme. *Structural and Multidisciplinary Optimization* 55 (6):2045–72. doi:10.1007/s00158-016-1627-7.